



# SrTiO<sub>3</sub> single crystals enclosed with high-indexed {023} facets and {001} facets for photocatalytic hydrogen and oxygen evolution

Bin Wang, Shaohua Shen<sup>\*</sup>, Liejin Guo<sup>\*</sup>

International Research Centre for Renewable Energy, State Key Laboratory of Multiphase Flow in Power Engineering, Xi'an Jiaotong University, Shaanxi 710049, China

## ARTICLE INFO

### Article history:

Received 31 August 2014

Received in revised form 8 November 2014

Accepted 15 November 2014

Available online 22 November 2014

### Keywords:

SrTiO<sub>3</sub> single crystals

High-indexed facets

Photocatalysis

Hydrogen production

Oxygen production

## ABSTRACT

SrTiO<sub>3</sub> single crystals enclosed with high-indexed {023} facets and {001} facets were facilely synthesized *via* a one-pot solvothermal method. The ratio of {023} to {001} facets could be simply adjusted by tuning the NaOH and EA concentrations during the solvothermal growth process. It was demonstrated that the photocatalytic activities of the variously shaped SrTiO<sub>3</sub> should be closely related to the morphology of SrTiO<sub>3</sub>, *i.e.*, the ratio of {023} to {001} facet. The highest photocatalytic activities are achieved for SrTiO<sub>3</sub> single crystals with the ratio of {023} to {001} facet tuned to 35:65, with hydrogen and oxygen evolution rates reaching 71.1 and 30.0 μmol/h, respectively, which are about 9.5 and 3.0 times higher than those of the irregular SrTiO<sub>3</sub> particles. Facet selective photo-deposition of metal ions reveals that the high-indexed {023} facets provided active sites for photo-oxidation reaction, while the {001} facets offered active sites for photo-reduction reaction. Such spatially separated photoactive reduction and oxidation sites should benefit charge separation in a SrTiO<sub>3</sub> single crystal, leading to higher photocatalytic activity related to the irregular SrTiO<sub>3</sub> particles.

© 2014 Elsevier B.V. All rights reserved.

## 1. Introduction

Semiconductor based photocatalytic water splitting has been widely accepted as an alternative approach to producing high-purity hydrogen, addressing the unprecedented increases of world energy and environment demands. The key to this technology is the development of promising photocatalysts in terms of both high activity and good stability for hydrogen production via water splitting [1]. Among the various photocatalysts, strontium titanate (SrTiO<sub>3</sub>) has been one of the most attractive candidates due to its high photoactivity, low cost and excellent chemical stability [2].

To achieve the good photoreactivity, it is of crucial importance to make charge carriers effectively separate and transfer to the surface active sites. To this end, numerous approaches have been attempted to promote charge separation [3–6]. Among them, coupling of two different materials by forming heterojunctions at the interfaces has been demonstrated with great success [7,8]. For example, CdS/TiO<sub>2</sub> [9], TiO<sub>2</sub>/BiVO<sub>4</sub> [10], Fe<sub>2</sub>O<sub>3</sub>/Si [11], and TiO<sub>2</sub>/Si [12,13], *etc.*, have been developed to show much higher photocatalytic activities than their single component counterparts.

Su *et al.* reported that WO<sub>3</sub>/BiVO<sub>4</sub> heterojunction showed much higher photocatalytic activity than the individual WO<sub>3</sub> and BiVO<sub>4</sub> counterpart for solar water splitting. It was proposed that the heterojunctions between WO<sub>3</sub> and BiVO<sub>4</sub> can efficiently separate the photogenerated electrons and holes, hence enhancing the photoconversion efficiency [14]. Recently, it was demonstrated that efficient charge separation can be realized over single crystal semiconductor photocatalysts [15–18]. The photocatalytic activity greatly relies on the surface structure and exposed crystal facets of a given photocatalyst. For example, Li *et al.* reported that photo-generated electrons and holes can be separated at two different crystals facets, *i.e.*, {010} and {110} facets, for a well-shaped BiVO<sub>4</sub> single-crystal [15]. Similar phenomena of charge separation between different crystal facets have also been reported for various TiO<sub>2</sub> single crystals [16,18–20]. Majima *et al.* successfully probed the surface-energy-independent distribution of available reactive sites within one TiO<sub>2</sub> crystal using spatially and temporally resolved fluorescence measurements with single-molecule redox sensors [17]. They found that the reaction sites for the effective reduction of the probe molecules are preferentially located on the {101} facets rather than the {001} facets with a higher surface energy. Matsumura *et al.* demonstrated that Pt and PbO<sub>2</sub> particles can be photo-deposited on the {110} and {011} facets of a rutile TiO<sub>2</sub> crystal, respectively. This clearly indicated that the {110} and {011} facets could provide reduction and oxidation photoactive

<sup>\*</sup> Corresponding authors.

E-mail addresses: [shshen.xjtu@mail.xjtu.edu.cn](mailto:shshen.xjtu@mail.xjtu.edu.cn) (S. Shen), [lj-guo@mail.xjtu.edu.cn](mailto:lj-guo@mail.xjtu.edu.cn) (L. Guo).

sites, respectively, enhancing the separation of photo-introduced charges [16]. Liu *et al.* reported that the photoreactivity of {010} facets of  $\text{TiO}_2$  is higher than that of {101} facets, while {001} facets showed the lowest photoreactivity [20]. Recently, Zhang *et al.* discovered that the photo-introduced electrons and holes prefer to accumulate on high-indexed {054} facets and {001} facets of  $\text{Cu}_2\text{O}$ , respectively [21]. Huang *et al.* reported that high-index faceted concave cubic  $\text{AgCl}$  showed higher photocatalytic activity in  $\text{O}_2$  evolution than flat {001} enclosed cubic  $\text{AgCl}$  [22]. Thus, high-index faceted nanocrystals may deserve special attention as they usually provide atomic kinks and steps (more active) on the crystal surfaces, leading to enhanced photoreactivity.

To date, different methods such as solution-phase decomposition and hydrothermal process, have been developed to synthesize shape controlled  $\text{SrTiO}_3$  including rods [23], eight-pod star-shape [24], cube-like shape [25], spheres and flakes [26]. However, precise control in terms of  $\text{SrTiO}_3$  single crystal enclosed with high-indexed facets is still limited. In this study, we successfully synthesized uniform nanosized  $\text{SrTiO}_3$  single-crystals enclosed with high-indexed {023} facets and low-indexed {001} facets via a facile solvothermal method, and their photocatalytic activities for hydrogen and oxygen production from water, depending on the ratio of {023} to {001} facets, were investigated in detail. It was demonstrated that the promoted charge separation on the faceted  $\text{SrTiO}_3$  single crystals, with photo-induced reduction occurring at the {001} facets and oxidation at the high-indexed {023} facets, respectively, greatly contributed to the much higher photocatalytic activity related to the irregular  $\text{SrTiO}_3$  particles.

## 2. Experimental

### 2.1. Samples preparation

$\text{SrTiO}_3$  enclosed with high-indexed {023} facets and {001} facets was synthesized by a facile one-pot solvothermal method with controlled concentrations of ethanolamine (EA) and sodium hydroxide (NaOH). In a typical process, 10 mmol of tetrabutyl titanate was dissolved into 20 mL of EA to form a transparent light yellow solution, and then 50 mL of NaOH aqueous solution was dropped to obtain a white precipitate suspension. 10 mL of aqueous solution containing 10 mmol of  $\text{Sr}(\text{NO}_3)_2$  was added into the suspension under stirring. The total volume of the final suspension solution was maintained 80 mL. The final suspension solution was then sealed in a 100 mL Teflon-lined stainless steel autoclave, followed by heat treatment at  $180^\circ\text{C}$  for 24 h. After cooling, the resulted white precipitates were centrifuged and washed with ethanol and deionized water for several times, respectively, and dried under vacuum at  $80^\circ\text{C}$  for 10 h. By tuning the concentrations of NaOH (1.5, 3, and 9 M) and EA (25, and 50 vol%) in the final suspension solution, the obtained  $\text{SrTiO}_3$  samples were designed as STO- $x\text{M}-y\text{EA}$  ( $x = 1.5, 3, 9$ ;  $y = 25, 50$ ).

### 2.2. Characterization

The X-ray diffraction (XRD) patterns were obtained from a PANalytical X'pert MPD Pro diffractometer operated at 40 kV and 40 mA using Ni-filtered  $\text{Cu K}\alpha$  irradiation (Wavelength 1.5406 Å). UV–vis absorption spectra (UV–vis) were measured on a HITACHI U4100 instrument equipped with labsphere diffuse reflectance accessory using  $\text{BaSO}_4$  as the reference.  $\text{N}_2$  adsorption–desorption isotherms were conducted at 77 K using an Accelerated Surface Area and Porosimetry Analyzer (ASAP 2020, Micromeritics) after degassing the samples at  $150^\circ\text{C}$  for 2 h. Surface area was determined using the Brunauer–Emmett–Teller (BET) methods. A JSM-7800F instrument (JEOL) was used to perform field emission scanning electron

microscopy (FE-SEM). An OXFORD INCA energy-dispersive X-ray detector (EDX) which was mounted in the above FE-SEM was used to conduct elemental analysis. The transmission electron microscopy (TEM) images were obtained from a FEI Tecnai G2 F30 S-Twin transmission electron microscope at an accelerating voltage of 300 kV. X-ray photoelectron spectroscopy (XPS) measurements were conducted on a Kratos spectrometer (AXIS Ultra DLD) with monochromatic Al  $\text{K}\alpha$  radiation ( $h\nu = 1486.69\text{ eV}$ ), and with the pressure of sample analysis chamber under high vacuum ( $<3 \times 10^{-9}$  Torr). All binding energies were referenced to the C 1s peak at 284.8 eV.

### 2.3. Photocatalytic activity evaluation

For photocatalytic hydrogen (or oxygen) evolution, 0.1 g of photocatalyst powder was dispersed into 220 mL of 20 vol%  $\text{CH}_3\text{OH}$  (40 mmol of  $\text{KIO}_3$  for oxygen evolution) aqueous solution under stirring in a side-irradiation photoreactor. The suspension was irradiated with 300 W Xe lamp with reaction temperature maintained at  $35^\circ\text{C}$  by thermostatic water bath. Before the photocatalytic reaction, nitrogen was purged through the reactor for 15 min to ensure complete removal of oxygen. The amount of  $\text{H}_2$  or  $\text{O}_2$  gas was determined using online thermal conductivity detector (TCD) gas chromatography (NaX zeolite column, TCD detector,  $\text{N}_2$  carrier). For photocatalytic hydrogen evolution, 0.5 wt% Pt as co-catalysts were loaded onto the surface of the as-prepared photocatalysts by an in situ photo-deposition method, with an appropriate amount of  $\text{H}_2\text{PtCl}_6 \cdot 6\text{H}_2\text{O}$  as Pt precursor.

### 2.4. Photocatalytic deposition of Pt and $\text{PbO}_2$

Photo-deposition of 5 wt% Pt and  $\text{PbO}_2$  on the surfaces of  $\text{SrTiO}_3$  were carried out using  $\text{H}_2\text{PtCl}_6$  and  $\text{Pb}(\text{NO}_3)_2$  as precursors, respectively. Typically, 0.2 g of  $\text{SrTiO}_3$  powder and a calculated amount of metal precursor were mixed in 220 mL of deionized water under stirring. The suspension was then irradiated by a 300-W Xe lamp with reaction temperature maintained at  $35^\circ\text{C}$  by thermostatic water bath. After 5 h photo-deposition, the suspension was filtered, washed with deionized water for five times, and finally dried under vacuum at  $80^\circ\text{C}$  for 10 h. For photo-deposition of Pt and  $\text{PbO}_2$ , methanol and  $\text{KIO}_3$  were used as electron donors and acceptors, respectively.

## 3. Results and discussion

Typically,  $\text{SrTiO}_3$  nanocrystals were obtained via a solvothermal procedure by heating a mixture solution containing NaOH, EA,  $\text{Sr}(\text{NO}_3)_2$  and tetrabutyl titanate at  $180^\circ\text{C}$  for 24 h. Fig. 1 schemes the synthesis of  $\text{SrTiO}_3$  nanocrystals with different shapes. Various shaped  $\text{SrTiO}_3$ , e.g., irregular particles, cube and tetrahexahedron crystals, and cubic crystals, were obtained by facily adjusting the concentrations of EA and NaOH in precursor solutions. To visualize the morphological evolution of  $\text{SrTiO}_3$ , representative SEM images of  $\text{SrTiO}_3$  prepared under different synthetic conditions were taken. As shown in Fig. 2a, irregular  $\text{SrTiO}_3$  particles with rough surfaces were obtained in the solution of 1.5 M NaOH and 25 vol% EA (STO-1.5M-25EA). Interestingly, the irregular particles then changed into cube and tetrahexahedron [27] with high-indexed {023} facets and low-indexed {001} facets exposed by increasing the NaOH concentration to 3 M (STO-3M-25EA, Fig. 2b). The {023} and {001} facets could be confirmed by high-resolution TEM images, which will be discussed later. With the concentration of NaOH (3 M) unchanged while that of EA increased to 50 vol%, the shape of the obtained  $\text{SrTiO}_3$  nanocrystals remained in cube and tetrahexahedron, while the ratio of exposed {023} to {001} facets became smaller for the obtained STO-3M-50EA (Fig. 2c) than

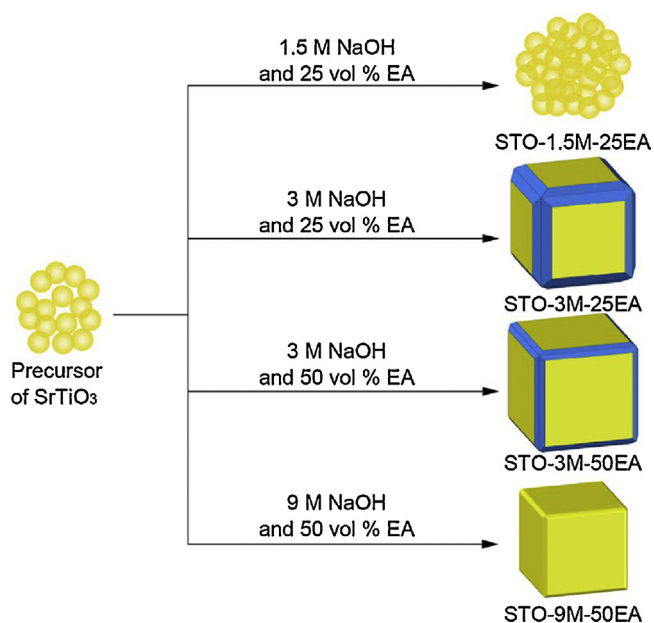


**Fig. 1.** Schematic processes for the synthesis of SrTiO<sub>3</sub> nanocrystals with different shapes by varying the synthetic conditions.

those of STO-3M-25EA. The morphology of SrTiO<sub>3</sub> nanocrystals was then transformed into perfect cube with only {001} facets exposed (Fig. 2d) by further increasing the concentration of NaOH to 9 M (STO-9M-50EA). In short, in this case the ratio of {023} to {001} facets of SrTiO<sub>3</sub> single crystals could be easily tuned by changing

the NaOH and EA concentrations during the solvothermal growth process.

The UV–vis absorption spectra of the SrTiO<sub>3</sub> samples are given in Figure S1 (see Supplementary material). The band gaps of all the samples were determined to be ca. 3.20 eV by the Kubelka–Munk method [28]. This indicated that the different morphologies of these SrTiO<sub>3</sub> samples had little effect on their band gaps, and the light absorption ability of the samples should not be related to their varied photoactivities. Figure S2 (see Supplementary material) shows the XRD patterns of the variously shaped SrTiO<sub>3</sub> samples. The XRD peak positions were consistent for all the four samples, and no impurity peaks were observed, confirming the pure SrTiO<sub>3</sub> of cubic-phase perovskite structure (JCPDS No. 00-035-0734, space group: *Pm*-3*m*). The concentrations of NaOH and EA had little effect on the crystal structures of SrTiO<sub>3</sub> in the present solvothermal condition. Surface area of the as-prepared SrTiO<sub>3</sub> samples were measured and listed in Table S1. There is no significant difference in the BET surface area of these samples, indicating that the surface area should not be related to their various photocatalytic activities.

The {023} and {001} facets of the cube and tetrahexahedron SrTiO<sub>3</sub> nanocrystals were confirmed by high-resolution TEM images. Fig. 3a shows the typical TEM image of STO-3M-25EA, displaying a twelve-side polygon viewed from the *a*-axis direction. HRTEM image (Fig. 3a, inset) recorded from the dotted circular area (i) gives two sets of lattice fringes with the same spacing of 2.76 Å and the included angle of 90°, corresponding to the (011) and (01-1) planes of cubic SrTiO<sub>3</sub>, respectively. Therefore, the top facet of the nanocrystal in Fig. 3a can be confirmed as the (100) facet. Fig. 3b is the magnified TEM image of the dotted circular area (ii) in Fig. 3a. The interior angles of the twelve-side polygon are divided into two categories, one is 157.4° and the other is 147.4°. According to Steno's law, for crystals of different shapes and sizes,

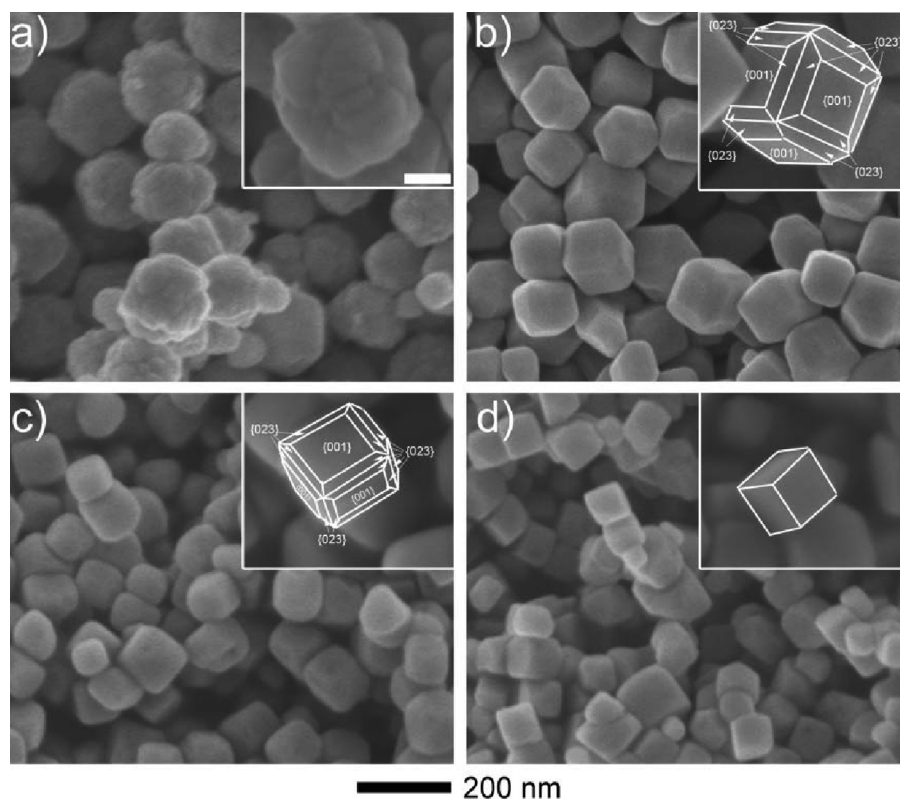


**Fig. 2.** SEM images of SrTiO<sub>3</sub> nanocrystals. (a) STO-1.5M-25EA, (b) STO-3M-25EA, (c) STO-3M-50EA, (d) STO-9M-50EA. The scale bar in the inset of (a) is 50 nm and also applied to the other insets.



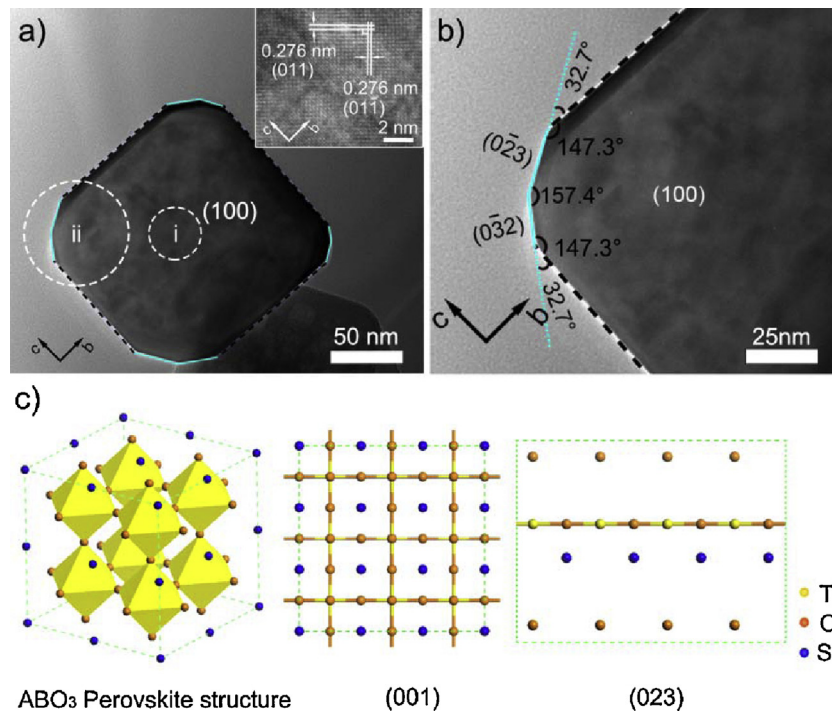


**Fig. 3.** (a) TEM of the STO-3M-25EA sample with large {023} facets, the inset is the HRTEM image recorded from the dotted circular area (i), (b) magnified TEM of the dotted circular area (ii) in Fig. 2a, (c) 3D projection of the SrTiO<sub>3</sub> of perovskite structure, and the atomic models of SrTiO<sub>3</sub> microstructures viewed from [001] and [023] directions.

the included angle of two specific planes is constant. Then, the exposed high index facets can be well defined as {023}, according to the equation of included angle for a cubic system (Eq. (1)).

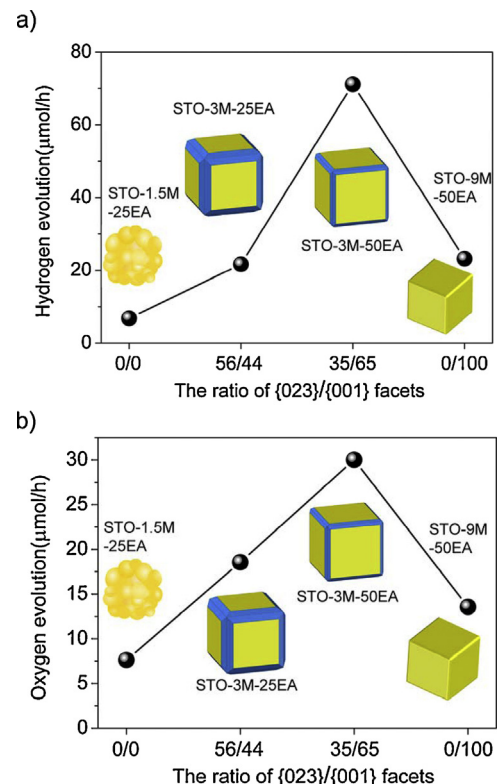
$$\cos \theta = \frac{h_1 h_2 + k_1 k_2 + l_1 l_2}{\sqrt{h_1^2 + k_1^2 + l_1^2} \sqrt{h_2^2 + k_2^2 + l_2^2}} \quad (1)$$

Fig. 3c displays the 3D projection of the SrTiO<sub>3</sub> of ABO<sub>3</sub> perovskite structure, and the atomic models of SrTiO<sub>3</sub> viewed from [001] and [023] directions, respectively. The {001} surface of SrTiO<sub>3</sub> is terminated by either TiO<sub>2</sub> or SrO layer, while the atomic arrangement and coordination of {023} facet is very different from that of the {001} facet as illustrated in Fig. 3c. The ratios of {023} to {001} facets for these different cube and tetrahexahedron SrTiO<sub>3</sub> nanocrystals could be determined from the TEM images of SrTiO<sub>3</sub> nanocrystals (Figure S3, Supplementary material), which are listed in Table 1.

It was demonstrated that surface atomic structures will intrinsically affect the transfer and separation of photoexcited charges on the crystal surfaces, and hence the activity of photocatalyst [13]. Thus, the different surface atomic structures between {001} and {023} facets may be responsible for the charge transfer and separation during photocatalytic reaction and affect the photocatalytic activities, which will be discussed in the following section.

Fig. 4 shows the photocatalytic hydrogen and oxygen production rates over the as-prepared SrTiO<sub>3</sub> samples. For both hydrogen (Fig. 4a) and oxygen (Fig. 4b) evolution, the

photocatalytic activities are very low for the irregular SrTiO<sub>3</sub> particles (STO-1.5M-25EA), with hydrogen and oxygen evolution rates to be only 6.8 and 7.6 μmol/h, respectively. When the SrTiO<sub>3</sub> nanocrystals are exposed with {023} facets together with {001} facets, the STO-3M-25EA sample shows dramatically increased



**Fig. 4.** The photocatalytic performances of (a) H<sub>2</sub> and (b) O<sub>2</sub> production over various shaped SrTiO<sub>3</sub> nanocrystals.

**Table 1**

Average percentages of {023} and {001} facets in various shaped SrTiO<sub>3</sub> samples, calculated from the surface area of exposed facets from TEM images (Figure S3, Supplementary material).

Sample	{023}	{001}	{023}/{001}
STO-1.5M-25EA	–	–	–
STO-3M-25EA	56%	44%	56/44
STO-3M-50EA	35%	65%	35/65
STO-9M-50EA	0	100%	0/100

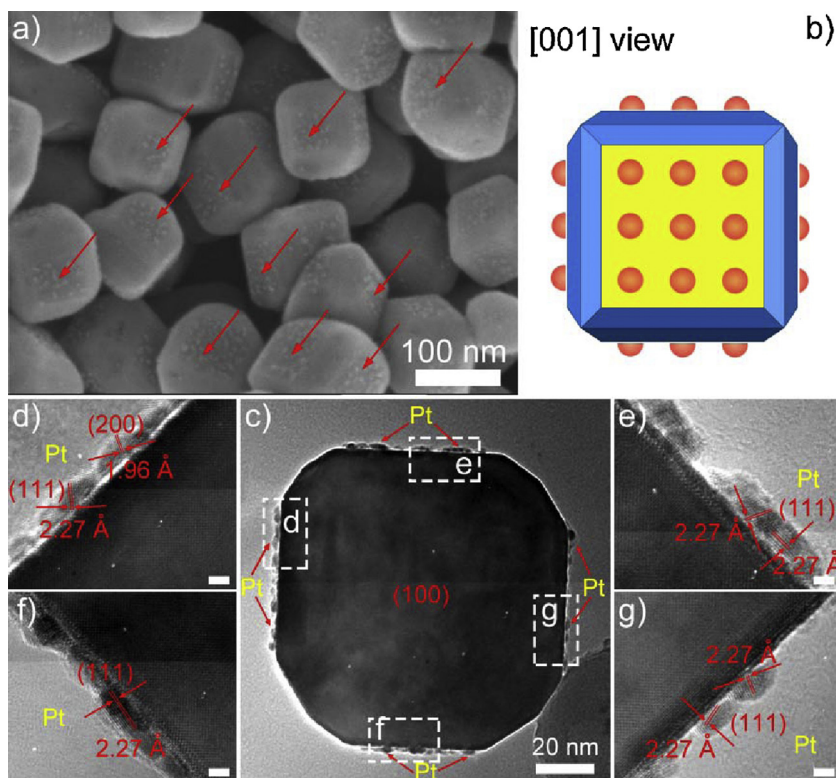


**Fig. 5.** (a) SEM image of SrTiO<sub>3</sub> (STO-3M-25EA) loaded with 5 wt% Pt; (b) 3-dimensional models of a single SrTiO<sub>3</sub> nanocrystal loaded Pt particles viewed in [001] direction; (c) TEM image of a single SrTiO<sub>3</sub> nanocrystal loaded Pt particles viewed in [001] direction; (d)–(g) HRTEM of the corresponding dotted rectangular area d, e, f, g in (c), scale bars in d–g are 2 nm.

photocatalytic activities for both hydrogen and oxygen evolution. With the ratio of exposed {023} to {001} facets decreases, a further increase in photocatalytic activities are achieved for STO-3M-50EA, with photocatalytic hydrogen and oxygen evolution rates reaching 71.1 and 30.0  $\mu\text{mol/h}$ , respectively, which are about 9.5 and 3.0 times higher than those of the irregular SrTiO<sub>3</sub> particles (STO-1.5M-25EA). However, when the {023} facets disappear, the STO-9M-50EA sample shows lower photocatalytic activities than those cube and tetrahexahedron SrTiO<sub>3</sub> nanocrystals enclosed with both {023} and {001} facets.

It has been clearly demonstrated that the photocatalytic activity of these obtained SrTiO<sub>3</sub> crystals should be closely related to their various morphologies, i.e., the ratio of {023} to {001} facets. Tsang *et al.* reported that the ratio of different crystal facets exposed on the crystal surface had significant effects on the photocatalytic activity of ZnO for the decomposition of methylene blue in aqueous solution [29], and it was indicated that a greater proportion of exposed polar {001} facets led to greater photocatalytic activity. Pradhan *et al.* reported that the presence of both high-energy {001} oxidative and low-energy {101} reductive facets in an optimal ratio was necessary to reduce charge recombination and thereby enhance the photocatalytic activity of TiO<sub>2</sub> nanocrystals [30]. Therefore, in the present study, it could be supposed that there should be preferential separation and distribution of electrons and holes on {001} and {023} facets, respectively.

In order to verify this assumption, Pt and PbO<sub>2</sub> were selectively photo-deposited on SrTiO<sub>3</sub> by the in situ photo-deposition method, which can probe the photo-reaction sites by determining the crystal facets for the photo-reductive or photo-oxidative deposition of metals or metal oxides. As clearly shown in Fig. 5a, Pt was loaded on {001} facets, as schemed in Fig. 5b. Representative TEM image of the SrTiO<sub>3</sub> photocatalyst after Pt photo-deposition reaction was shown in Fig. 5c. This again confirmed that Pt particles with ~5 nm

in diameter were loaded on {001} facets, whereas no Pt particles were loaded on {023} facets. To further identify the existence of Pt on the {001} facets, the dotted rectangular area d–g in Fig. 5c were magnified, as shown in Fig. 5d–g. The lattice spaces of the nanoparticles loaded onto the surface of SrTiO<sub>3</sub> crystals were determined to be 1.96 and 2.27 Å, corresponding to the (200) and (111) lattice spaces of Pt metal, respectively. Fig. 6a shows the SEM image of SrTiO<sub>3</sub> after PbO<sub>2</sub> photo-deposition reaction. PbO<sub>2</sub> particles were found on {023} facets, as schemed in Fig. 6b. TEM image of the SrTiO<sub>3</sub> loaded with 5 wt% PbO<sub>2</sub> was shown in Fig. 6c. It is clearly verified that PbO<sub>2</sub> particles (10–20 nm) were only deposited on {023} facets. Fig. 6d–g shows the HRTEM images recorded from the dotted rectangular area d–g in Fig. 6c. The lattice spacings measured to be 3.12 and 2.97 Å corresponds to (111) and (020) lattice plane of PbO<sub>2</sub>, respectively. EDX and XPS analysis further confirmed the successful photo-deposition of Pt and PbO<sub>2</sub> on SrTiO<sub>3</sub> single crystals (Figure S4, Supplementary material). Given the photodeposition of Pt and PbO<sub>2</sub> via surface reduction and oxidation reaction occurring at {001} and {023} facets, respectively, these experimental results clearly demonstrated that the photogenerated electrons and holes could be separated and migrated to different facets of as-prepared SrTiO<sub>3</sub> nanocrystals, and the {001} and {023} facets prefer the reduction and oxidation reactions, respectively.

The photo-induced charge separation processes over {001} and {023} facets could be proposed and described in Fig. 7. As validated by the experiments of selective photodeposition of Pt and PbO<sub>2</sub>, the photo-excited electrons and holes could effectively separate and transfer to the {001} and {023} facets, respectively, and then get involved in surface photo-reduction and oxidation reactions (Fig. 7a). Therefore, the higher photocatalytic activity of the cube and tetrahexahedron SrTiO<sub>3</sub> sample related to the irregular SrTiO<sub>3</sub> particulate sample should be due to the promoted charge transfer and separation at the spatially separated photoactive sites

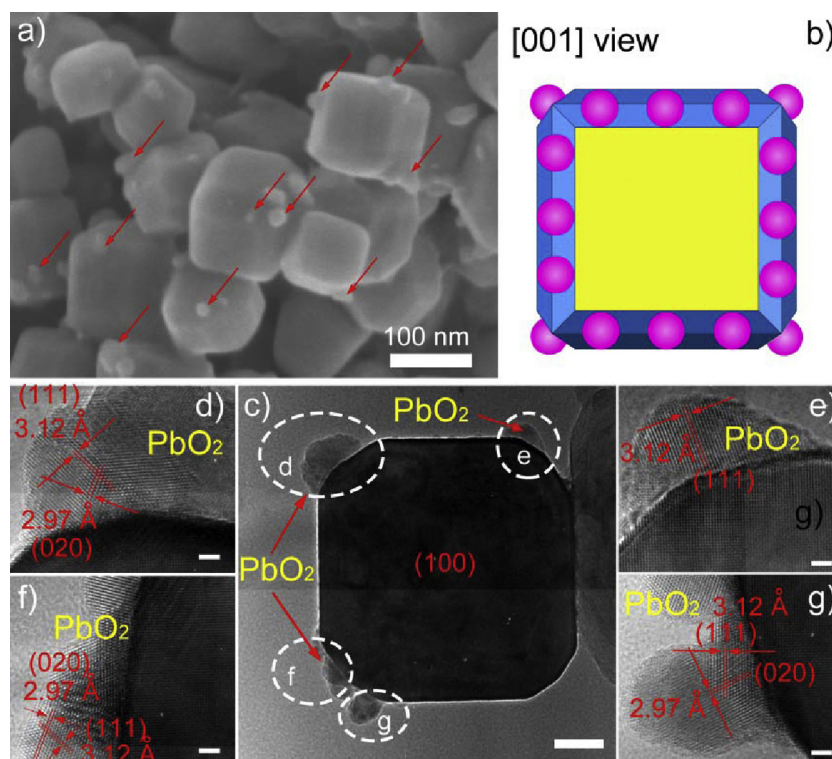


**Fig. 6.** (a) SEM image of SrTiO<sub>3</sub> (STO-3M-25EA) loaded with 5 wt% PbO<sub>2</sub>; (b) 3-dimensional models of a single SrTiO<sub>3</sub> nanocrystal loaded PbO<sub>2</sub> particles viewed in [001] direction; (c) TEM image of a single SrTiO<sub>3</sub> nanocrystal loaded PbO<sub>2</sub> particles viewed in [001] direction; (d)–(g) HRTEM of the corresponding dotted rectangular area d, e, f, g in (c), scale bars in d–g are 2 nm.

at {001} and {023} facets for water reduction and oxidation reaction, respectively (Fig. 7b). In addition, the optimized ratio of {001} to {023} facets results in the competitive balance of the numbers of reduction and oxidation active sites on {001} and {023} facets,

and hence the highest photocatalytic activities for hydrogen and oxygen evolution, respectively.

#### 4. Conclusions

In summary, we successfully synthesized SrTiO<sub>3</sub> single crystals enclosed with high-indexed {023} facets and {001} facets via a one-pot solvothermal method, and found that the photocatalytic hydrogen and oxygen production activities were greatly dependent on the ratio of {023} and {001} facets. By tuning the ratio of {023} to {001} facets, the relatively high photocatalytic activities were achieved for the cube and tetrahexahedron SrTiO<sub>3</sub> nanocrystals, with hydrogen and oxygen evolution rates reaching 71.1 and 30.0 μmol/h, respectively, which are about 9.5 and 3.0 times higher than those of irregular SrTiO<sub>3</sub> particles. It was confirmed that the spatial separation of photoreduction and photooxidation active sites at different facets of the SrTiO<sub>3</sub> nanocrystals, as evidenced by facet-selective photo-deposition of metals and oxides, led to the promoted charge separation between {001} and {023} facets. As a result, the enhanced photocatalytic activities for hydrogen and oxygen generation were achieved, and an appropriate ratio of {001} and {023} facets for reduction and oxidation reaction could lead to a further increase in photocatalytic activity.

#### Acknowledgements

The authors gratefully acknowledge the financial supports from the National Natural Science Foundation of China (No. 51102194, No. 51323011, No. 51121092), the Natural Science Foundation of Shaanxi Province (No. 2014KW07-02) and the Natural Science Foundation of Jiangsu Province (No. BK20141212) and the Nano Research Program of Suzhou City (No. ZXG201442, No. ZXG2013003). S. Shen is supported by the Foundation for the Author of National Excellent Doctoral Dissertation of P.R. China

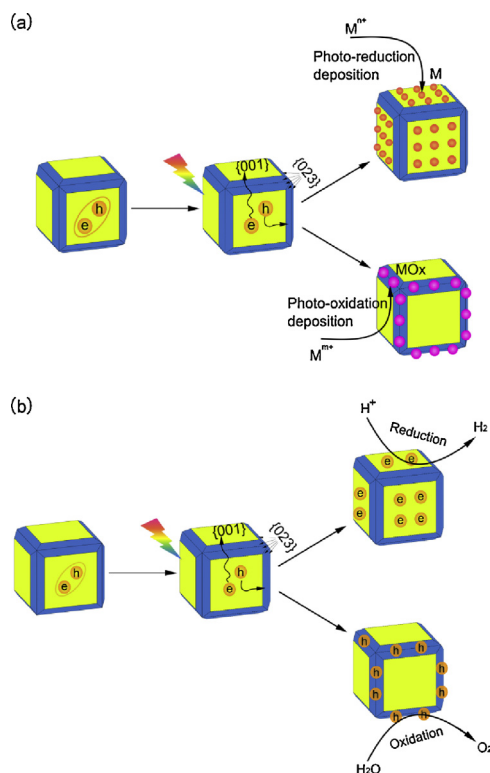


**Fig. 7.** Plausible mechanisms of the photoinduced charge separation process on {001} and {023} facets.



(No. 201335) and the “Fundamental Research Funds for the Central Universities”.

## Appendix A. Supplementary data

Supplementary data associated with this article can be found, in the online version, at <http://dx.doi.org/10.1016/j.apcatb.2014.11.032>.

## References

- [1] X. Chen, S. Shen, L. Guo, S.S. Mao, *Chem. Rev.* 110 (2010) 6503–6570.
- [2] J. Shi, L. Guo, *Nat. Sci. Mater. Int.* 22 (2012) 592–615.
- [3] M. Liu, D. Jing, Z. Zhou, L. Guo, *Nat. Commun.* 4 (2013) 2278–2285.
- [4] X. Xu, C. Randorn, P. Efsthathiou, J.T. Irvine, *Nat. Mater.* 11 (2012) 595–598.
- [5] X. Chen, L. Liu, Y.Y. Peter, S.S. Mao, *Science* 331 (2011) 746–750.
- [6] M. Liu, L. Wang, G.M. Lu, X. Yao, L. Guo, *Energy Environ. Sci.* 4 (2011) 1372–1378.
- [7] M.T. Mayer, Y. Lin, G. Yuan, D. Wang, *Acc. Chem. Res.* 46 (2013) 1558–1566.
- [8] X. Zong, H. Yan, G. Wu, G. Ma, F. Wen, L. Wang, C. Li, *J. Am. Chem. Soc.* 130 (2008) 7176–7177.
- [9] D. Kannaiyan, E. Kim, N. Won, K.W. Kim, Y.H. Jang, M.-A. Cha, D.Y. Ryu, S. Kim, D.H. Kim, *J. Mater. Chem.* 20 (2010) 677–682.
- [10] M. Xie, X. Fu, L. Jing, P. Luan, Y. Feng, H. Fu, *Adv. Energy Mater.* 4 (2014), <http://dx.doi.org/10.1002/aenm.201300995>.
- [11] M.T. Mayer, C. Du, D. Wang, *J. Am. Chem. Soc.* 134 (2012) 12406–12409.
- [12] I.S. Cho, Z. Chen, A.J. Forman, D.R. Kim, P.M. Rao, T.F. Jaramillo, X. Zheng, *Nano Lett.* 11 (2011) 4978–4984.
- [13] J. Shi, X. Wang, *Energy Environ. Sci.* 5 (2012) 7918–7922.
- [14] J. Su, L. Guo, N. Bao, C.A. Grimes, *Nano Lett.* 11 (2011) 1928–1933.
- [15] R. Li, F. Zhang, D. Wang, J. Yang, M. Li, J. Zhu, X. Zhou, H. Han, C. Li, *Nat. Commun.* 4 (2013) 1432–1439.
- [16] T. Ohno, K. Sarukawa, M. Matsumura, *New J. Chem.* 26 (2002) 1167–1170.
- [17] T. Tachikawa, S. Yamashita, T. Majima, *J. Am. Chem. Soc.* 133 (2011) 7197–7204.
- [18] H.G. Yang, C.H. Sun, S.Z. Qiao, J. Zou, G. Liu, S.C. Smith, H.M. Cheng, G.Q. Lu, *Nature* 453 (2008) 638–641.
- [19] G. Liu, C.Y. Jimmy, G.Q.M. Lu, H.M. Cheng, *Chem. Commun.* 47 (2011) 6763–6783.
- [20] J. Pan, G. Liu, G.Q.M. Lu, H.M. Cheng, *Angew. Chem. Int. Ed.* 50 (2011) 2133–2137.
- [21] L. Zhang, J. Shi, M. Liu, D. Jing, L. Guo, *Chem. Commun.* 50 (2014) 192–194.
- [22] Z. Lou, B. Huang, X. Qin, X. Zhang, H. Cheng, Y. Liu, S. Wang, J. Wang, Y. Dai, *Chem. Commun.* 48 (2012) 3488–3490.
- [23] J.J. Urban, W.S. Yun, Q. Gu, H. Park, *J. Am. Chem. Soc.* 124 (2002) 1186–1187.
- [24] H. Xu, S. Wei, H. Wang, M. Zhu, R. Yu, H. Yan, J. Cryst. Growth 292 (2006) 159–164.
- [25] L.F. da Silva, W. Avansi, J. Andrés, C. Ribeiro, M.L. Moreira, E. Longo, V.R. Mastelaro, *Phys. Chem. Chem. Phys.* 15 (2013) 12386–12393.
- [26] T. Kimijima, K. Kanie, M. Nakaya, A. Muramatsu, *Appl. Catal. B* 144 (2014) 462–467.
- [27] W.E. Ford, *Dana's Manual of Mineralogy*, John Wiley, New York, 1912.
- [28] V. Kumar, S. Kr Sharma, T. Sharma, V. Singh, *Opt. Mater.* 12 (1999) 115–119.
- [29] A. McLaren, T. Valdes-Solis, G. Li, S.C. Tsang, *J. Am. Chem. Soc.* 131 (2009) 12540–12541.
- [30] N. Roy, Y. Sohn, D. Pradhan, *ACS Nano* 7 (2013) 2532–2540.